Multiscale analysis of the invariants of the velocity gradient tensor in isotropic turbulence

Mohammad Danish[*] and Charles Meneveau[†]

Department of Mechanical Engineering, Johns Hopkins University, Baltimore, Maryland 21218, USA

Knowledge of local flow-topology, the patterns of streamlines around a moving fluid element as described by the velocity-gradient tensor, is useful for developing insights into turbulence processes, such as energy cascade, material element deformation, or scalar mixing. Much has been learned in the recent past about flow topology at the smallest (viscous) scales of turbulence. However, less is known at larger scales, for instance, at the inertial scales of turbulence. In this work, we present a detailed study on the scale dependence of various quantities of interest, such as the population fraction of different types of flow-topologies, the joint probability distribution of the second and third invariants of the velocity gradient tensor, and the geometrical alignment of vorticity with strain-rate eigenvectors. We perform the analysis on a simulation dataset of isotropic turbulence at $Re_\lambda = 433$. While quantities appear close to scale invariant in the inertial range, we observe a "bump" in several quantities at length scales between the inertial and viscous ranges. For instance, the population fraction of unstable node-saddle-saddle flow topology shows an increase when reducing the scale from the inertial entering the viscous range. A similar bump is observed for the vorticity−strain-rate alignment. In order to document possible dynamical causes for the different trends in the viscous and inertial ranges, we examine the probability fluxes appearing in the Fokker-Plank equation governing the velocity gradient invariants. Specifically, we aim to understand whether the differences observed between the viscous and inertial range statistics are due to effects caused by pressure, subgrid-scale, or viscous stresses or various combinations of these terms. To decompose the flow into small and large scales, we mainly use a spectrally compact non-negative filter with good spatial localization properties (Eyink-Aluie filter). The analysis shows that when going from the inertial range into the viscous range, the subgrid-stress effect decreases more rapidly as a function of scale than the viscous effects increase. To make up for the difference, the pressure Hessian also behaves somewhat differently in the viscous than in the inertial range. The results have implications for models for the velocity gradient tensor showing that the effects of subgrid scales may not be simply modeled via a constant eddy viscosity in the inertial range if one wishes to reproduce the observed trends.

I. INTRODUCTION

The dynamical and statistical properties of velocity gradients in turbulent flows have elicited growing interest in recent years because velocity gradients provide a rich characterization of rotational and fluid deformation properties at the smallest, dynamically relevant scales of turbulence [1–3]. Deformation rates govern the dissipation of turbulent kinetic energy, while rotation rates characterize small-scale coherent vortical structures (worms) that are ubiquitous in turbulence [4–6].

---

[*]mohammad.danish@bennett.edu.in

[†]meneveau@jhu.edu

Conceptually, the dynamics of velocity gradients can be best understood in a Lagrangian frame following the flow [3,7,8]. The velocity gradient evolution along Lagrangian or inertial particle paths determines the dynamics of small (sub-Kolmogorov scale) objects moving, tumbling, and/or deforming with the flow such as bubbles and drops [9–11], polymers [12,13], and anisotropic particles [14–16]. And the velocity gradient tensor serves to characterize the local flow topology, which classifies the local flow structure based on the pattern of streamlines as seen by an observer translating (but not rotating) with a fluid element in a flow field. In incompressible turbulence, there exist four types of basic flow streamline topologies: stable-focus-stretching (SFS), unstable-focus-compressing (UFC), unstable-node-saddle-saddle (UNSS), and stable-node-saddle-saddle (SNSS) [1]. The type of flow topology can be uniquely determined by knowing the velocity gradient tensor (VGT) [1].

Since the pioneering work in Ref. [1], flow-topology-based analyses have been performed for both incompressible [2,17,18] as well as compressible turbulence [19,20]. Meanwhile, the outcomes of topology-based studies also provide benchmark results to be used in the assessment of predictive, reduced order models for the evolution equation of VGT [3,21–27].

Most of the prior work on velocity gradients deals with the smallest scales of turbulence since the velocity gradient in turbulence is dominated by the dynamics near the Kolmogorov scale. Analogous questions about the structure and local flow topology of turbulence can also be posed in the context of larger scales, for instance, in the inertial range of turbulence. Such questions have been addressed from the point of view of filtered velocity fields in Refs. [18,28] as well as from the fully Lagrangian viewpoint of particle tetrads separated by inertial-range distances ("perceived velocity gradients") in Refs. [24,29,30]. Recently a Lagrangian model for velocity gradients at arbitrarily high Reynolds numbers [31] has highlighted the need to better understand the dynamics and statistics of velocity gradients at all scales in turbulence. The initial version of the model assumed that inertial range and viscous range dynamics are similar (using the concept of a constant eddy viscosity in the inertial range). There are many reasons to doubt such a simplifying assumption. For example, consider the derivative skewness value in turbulence at multiple scales. In the viscous range, at moderate to high Reynolds numbers, and neglecting effects of intermittency, it is known to be about $\mathcal{S} = \langle(\partial u_1/\partial x_1)^3\rangle/\langle(\partial u_1/\partial x_1)^2\rangle^{3/2} \approx -0.5$. Conversely, in the inertial range the skewness is known to be of lower magnitude [32]. For instance, filtering the velocity at scale Δ in the inertial range (indicated by tildes) and using the assumption that $\partial \tilde{u}_1/\partial x_1 \sim [u(x + \Delta) - u(x)]/\Delta$ or, equivalently, the notion of "perceived velocity gradient," one may use the inertial range estimates $\langle[u(x + \Delta) - u(x)]^3\rangle \sim -(4/5)\epsilon\Delta$ and $\langle[u(x + \Delta) - u(x)]^2\rangle \sim C_2\epsilon^{2/3}\Delta^{2/3}$ where ϵ is the mean rate of dissipation (again neglecting intermittency corrections) with the Kolmogorov constant $C_2 \approx 2.1$. As a result, the skewness of the filtered velocity gradient (or structure function skewness) in the inertial range becomes $\mathcal{S}_\Delta = -4/5 C_2^{-3/2} \approx -0.26$, only about half of the value in the viscous range. Performing an analysis of filtered velocity gradients in turbulence, a value near -0.3 was obtained by Cerutti *et al.* [32]. While qualitatively the most important aspect (negative sign in skewness) is maintained across scales, quantitative differences in statistics of velocity gradients can be expected as a function of scale with certain trends in the inertial range transitioning to another behavior in the viscous range. Other qualitative similarities have been noted, such as the existence of a tear-drop-shaped joint probability distribution function (PDF) of velocity gradient invariants not only in the viscous range but also at larger scales [18,33]. However, a more in-depth quantitative analysis of such properties comparing them in the inertial and viscous ranges is needed to deepen our understanding and enable comparisons to models for the velocity gradient tensor at various scales.

With this need in mind, in this paper we study the following quantities over a range of scales ranging from large to inertial to viscous scales in incompressible isotropic turbulence: (1) the skewness of velocity derivatives, (2) the joint PDF of velocity gradient invariants Q and R, where Q and R are the second and third invariants of the velocity gradient tensor, (3) the population fraction of various flow topologies as characterized by the pair (R, Q), and (4) the geometrical alignment of vorticity with strain-rate eigenvectors. Finally, we aim to provide some insights into possible dynamical reasons for the observed behaviors by examining the probability fluxes appearing in the Fokker-Planck equation

that governs the single-time statistics of the velocity gradients. The data to be used in the analysis are from a direct numerical simulation (DNS) dataset at moderate-to-high Reynolds number.

The paper is organized as follows. Section II recalls the basic equations and provides required details on the flow-topology classification. In Sec. III we present the joint PDF of Q and R and quantify the total probability of a point in the flow to display a given type of topology (i.e., we quantify the population fractions). In Sec. IV we measure the flux of probability in phase space and distinguish between terms associated with pressure, viscous stresses and subgrid-scale stresses. These results help identify which terms are responsible for various observed phenomena at various scales. Finally, in Sec. V we provide a summary and conclusions from this work.

II. BACKGROUND

In this section, we present basic quantities related to velocity gradients in Navier-Stokes (NS) turbulence at various length scales that are to be studied in this work. A well-resolved numerical solution of NS equations (DNS) contains information on all scales ranging from the largest possible to the smallest scale (Kolmogorov scale η). Though the information of turbulence at η is readily available from DNS, information at scale $\Delta > \eta$ requires the DNS field to be coarse grained. In coarse graining (filtering), we convolve the DNS field with low-pass kernel G over a domain of length scale Δ and define a quantity with tildes as representing the filtered field at scale Δ, where $\Delta > \eta$. For instance, $\tilde{u}_i(\mathbf{x},t)$ represents the ith component ($i = 1,2,3$) of the filtered velocity field at position $\mathbf{x}$ and time t.

Many types of filters are available for *a priori* analysis of turbulence data, such as sharp-spectral, top-hat (box), and Gaussian, each of them associated with different functions for G [34]. Since the list of filters is long, they must be selected based on some criteria. We follow the criteria identified by Eyink and Aluie [35], who state that the filter should be (a) positive in real space, (b) sufficiently smooth so that derivatives of any order are well defined, and (c) decay sufficiently rapidly for large distances. Those authors proposed a new filter (we shall refer to it as the Eyink-Aluie filter) which complies, by construction, with these criteria. More details about the Eyink-Aluie filter to be used in the present analysis are provided in Appendix B.

Starting from the Navier-Stokes equations, application of the convolution yields the filtered NS equations (also commonly used in large eddy simulations)

$$\frac{\partial \widetilde{u}_i}{\partial t} + \widetilde{u}_j \frac{\partial \widetilde{u}_i}{\partial x_j} = -\frac{\partial \tilde{p}}{\partial x_i} + \nu \frac{\partial^2 \widetilde{u}_i}{\partial x_j \partial x_j} - \frac{\partial \tau_{ij}}{\partial x_j}, \tag{1}$$

where p and ν denote pressure (divided by density) and kinematic viscosity of the fluid, respectively, and τ_{ij} is the subgrid-scale tensor defined as

$$\tau_{ij} = \widetilde{u_i u_j} - \widetilde{u}_i \widetilde{u}_j. \tag{2}$$

Next, the evolution equation of a filtered (coarse-grained) velocity gradient tensor (VGT) is obtained by taking gradient of (1) [18,28]:

$$\frac{dA_{ij}}{dt} = -\underbrace{\left(A_{ik}A_{kj} - A_{lm}A_{ml}\frac{\delta_{ij}}{3}\right)}_{\text{RE}} - H_{ij}^{\text{PR}} - H_{ij}^{\text{VIS}} - H_{ij}^{\text{SGS}} \tag{3}$$

where $\frac{d}{dt}$ represents the time rate of change following a fluid element with the filtered velocity, and A_{ij} is the filtered velocity gradient tensor defined as

$$A_{ij} = \frac{\partial \widetilde{u}_j}{\partial x_i}. \tag{4}$$

(Note that for convenience, we do not place a tilde on the gradient, and so no filtered or unfiltered prefix will be used, but it is understood that it can be unfiltered or filtered at scale Δ depending on the context.) In Eq. (3) the acronyms RE, PR, VIS, and SGS stand for restricted Euler, deviatoric
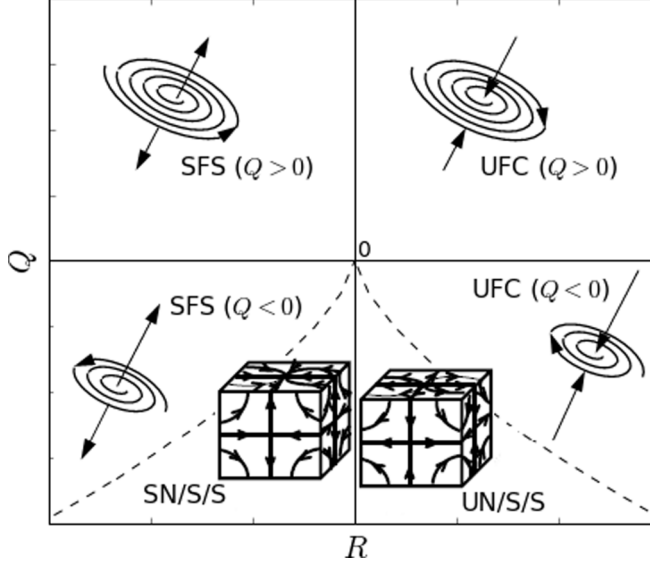
FIG. 1. Six zones and associated streamline patterns on the Q-R plane. Figure adapted from Refs. [18,19]. We distinguish also between positive and negative Q.

pressure Hessian, viscous diffusion Hessian, and Hessian involving subgrid stress, respectively. The three (trace-free) Hessian terms are defined as follows:

$$H_{ij}^{\text{PR}} = \frac{\partial^2 \widetilde{p}}{\partial x_i \partial x_j} - \frac{\delta_{ij}}{3} \frac{\partial^2 \widetilde{p}}{\partial x_k \partial x_k}, \quad H_{ij}^{\text{VIS}} = -\nu \frac{\partial^2 A_{ij}}{\partial x_k \partial x_k}, \quad H_{ij}^{\text{SGS}} = \frac{\partial^2 \tau_{jk}}{\partial x_i \partial x_k} - \frac{\delta_{ij}}{3} \frac{\partial^2 \tau_{mk}}{\partial x_m \partial x_k}. \quad (5)$$

Thus, at any scale larger than η, the evolution of the filtered VGT of a fluid element is dictated by the combined RE, PR, VIS, and SGS mechanisms. The SGS effect is expected to be significantly smaller than other terms when scale Δ becomes comparable to η, and similarly the VIS effect is expected to be quite small when Δ is sufficiently larger than η. On the other hand, the effects of RE and PR terms (self-stretching and rotation of gradients) are expected to persist no matter the scale.

A compact and convenient way to analyze the influence of these various terms on the filtered VGT as function of scales is to consider the VGT invariants, P, Q, and R, where

$$P = -A_{ii}, \quad Q = -\tfrac{1}{2} A_{ij} A_{ji} \quad \text{and} \quad R = -\tfrac{1}{3} A_{ij} A_{jk} A_{ki}. \quad (6)$$

In incompressible turbulence the first invariant will be identically zero ($P = 0$), whereas Q and R (of the filtered VGT) will evolve following the equations as obtained from (3) [2]:

$$\frac{dQ}{dt} = -3R + A_{ij} H_{ji}^{\text{PR}} + A_{ij} H_{ji}^{\text{VIS}} + A_{ij} H_{ji}^{\text{SGS}}, \quad (7)$$

$$\frac{dR}{dt} = \frac{2}{3} Q^2 + A_{ij} A_{jk} H_{ki}^{\text{PR}} + A_{ij} A_{jk} H_{ki}^{\text{VIS}} + A_{ij} A_{jk} H_{ki}^{\text{SGS}}. \quad (8)$$

The first terms, $3R$ and $2Q^2/3$, on right-hand side of Eqs. (7) and (8) are called restricted Euler (RE) terms.

Neglecting all terms except RE in Eqs. (7) and (8), Ref. [2] showed that typical initial conditions tend to a singularity in finite time following a universal behavior. Of special importance is the dynamical invariant (staying constant in time) of the RE system: $\frac{27}{4} R^2 + Q^3 = 0$. This equation represents two curves on the Q-R plane that osculate each other at the origin, as shown by dotted lines in Fig. 1 [1]. Note that the curve on the left side of Q axis is called a left-Vieillefosse tail, and the curve on the right side is called a right-Vieillefosse tail. These curves divide the Q-R plane into zones that display unique features of the velocity-gradient tensor. Specifically the VGT has complex eigenvalues if
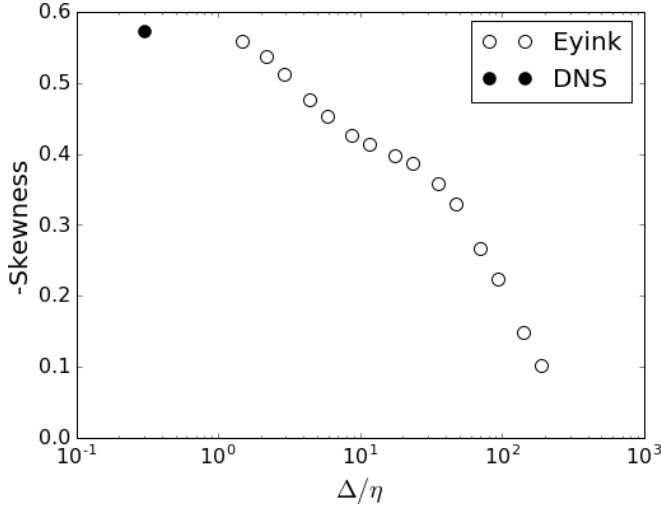
FIG. 2. Negative of longitudinal derivative skewness coefficient as function of filtering scale Δ/η in isotropic turbulence. The open symbols are from the filtered fields, and the solid circle is for the unfiltered DNS value (corresponding to a very small filtering scale so it is placed here arbitrarily somewhere at $\Delta/\eta < 1$).

falling in the upper zone (above the tails) and has all eigenvalues realed if VGT falls in the lower zone. Thus, the whole Q-R plane is divided into four different zones, each representing distinct patterns of streamlines (flow topology) as seen by an observer who is translating but not rotating with the fluid elements. These topologies are (1) stable-focus-stretching (SFS), (2) unstable-focus-compressing (UFC), (3) stable-node-saddle-saddle (SNSS), and (4) unstable-node-saddle-saddle (UNSS) [1]. We further divide the SFS and UFC topologies based on positive and negative values of Q, as $Q > 0$ means an enstrophy-dominated region and $Q < 0$ means a strain-dominated region (Fig. 1).

To date the joint PDF of Q-R has been used predominantly to study the small (viscous) scale behavior of turbulence [3]. From such studies, considerable insights about small-scale phenomena of turbulence have been obtained, like (1) the joint PDF of Q and R displays a peculiar, tear-drop-like, shape [2,17], (2) the tear-drop shape of a joint PDF has been found to exist in a variety of flows [36], (3) various zones of the Q-R plane has been found to occupy a certain fixed proportion in the turbulence field [19], and (4) the flow topology has been found to affect the alignment of vorticity and strain-rate eigenvectors [23], scalar dissipation [20], affecting, e.g., the "pirouette effect" [30,37,38].

Such statistics can also be obtained in the inertial range to develop better insights about turbulence across length scales. To obtain such statistics of Q and R for the velocity gradients at any length scale, the following calculations are performed:

(1) A DNS dataset of forced isotropic turbulence is downloaded from the database system to the compute environment. The data are from a 1024^3 DNS of forced isotropic turbulence [39]. Energy was injected by keeping the total energy constant in shells of radius, $|\kappa| \leqslant 2$. The Taylor-scale Reynolds number (Re_λ) is about 433. (2) The DNS velocity and pressure fields are transformed to Fourier space by performing three-dimensional (3D) fast Fourier transforms. (3) Fields are filtered at any desired scale by multiplying the filter's transfer function (we mostly use the Eyink-Aluie filter [35]; see Appendix B for more details). (4) Subsequently, the required gradients are evaluated from the filtered fields obtained in step (3) by multiplying by $i\mathbf{k}$, where $\mathbf{k}$ is the wave vector. (5) Finally, the gradient fields are computed back to physical space via inverse 3D Fourier transforms. Computations are performed using a notebook-based computational environment, physically located close to the data (SciServer; see Appendix A for more details).

We begin by showing, in Fig. 2, the averaged (negative) value of the longitudinal derivative skewness ($-S$) as a function of scale. The derivative skewness is computed here by taking the

average of the skewness in the three Cartesian directions, according to

$$S = \frac{1}{3}\left[\frac{\langle A_{11}^3 \rangle}{\langle A_{11}^2 \rangle^{3/2}} + \frac{\langle A_{22}^3 \rangle}{\langle A_{22}^2 \rangle^{3/2}} + \frac{\langle A_{33}^3 \rangle}{\langle A_{33}^2 \rangle^{3/2}}\right]. \tag{9}$$

In Fig. 2 the filled symbol shows the value obtained from the unfiltered field, and the open symbols are the values obtained from the filtered field. Here the unfiltered value has been shown at some small value of Δ/η. As shown in Fig. 2, the value of negative skewness increases from a small value at large scale to a value of 0.57 at the smallest scales. It should be noted that the value at the smallest possible filtered scale is almost same as that obtained from the unfiltered field. As reported earlier by in Ref. [32], we observe a distinct "bump" in going from the inertial range towards the viscous range. Similar bumps in structure function skewness have been observed before [40]. The precise value of the skewness within the inertial range also merits discussion. Using the Eyink-Aluie filter for the present dataset, we find skewness values in a range between -0.35 and -0.4, roughly speaking. We note that Ref. [32] (in its Fig. 13), reported values between -0.35 for a 3D spectral cutoff filter and -0.45 for a 3D Gaussian filter. Hence, present results are quite consistent with range of prior reported values. It must be recalled that the type of filter, as well as the Reynolds number, can affect the precise value of the skewness.

In the next section we explore whether such "bumps" between inertial and viscous range can also be observed for other properties of the velocity gradient tensor, such as the invariants Q and R and the population fractions.

III. STATISTICS OF Q AND R AS FUNCTION OF LENGTH SCALE

In this section, we present the statistics of Q and R in terms of their joint PDF, population fraction, etc., as computed from the flow field that has been filtered at various scales Δ. We consider a set of different filtering scales, which when expressed as multiples of the Kolmogorov scale η range from $[140, 93, \ldots, 2]$. These levels are selected individually to cover the transition between the inertial range and the viscous range (which is typically expected to occur below about 20η depending on how the transition is defined).

For presentation purposes, the invariants Q and R are normalized by $\langle Q_W \rangle$ and $\langle Q_W \rangle^{3/2}$, where $\langle \rangle$ represents global spatially averaged value and Q_W is the second invariant of rotation-rate tensor (W), given by

$$W_{ij} = \tfrac{1}{2}(A_{ij} - A_{ji}) \quad \text{and} \quad Q_W = \tfrac{1}{2}W_{ij}W_{ij}. \tag{10}$$

Note that, like VGT, we do not put prefix filtered or unfiltered to W_{ij} and its second invariant, but it is understood that they can be unfiltered or filtered at scale Δ depending on the context.

A. Isoprobability contours of joint PDF of Q and R

In Fig. 3 we plot isoprobability contours of the joint PDF of Q and R at its discrete levels 0.1, 0.01, 0.0032, and 0.001. Each plot in Fig. 3 shows contours at a fixed probability level for all filtering scales considered in this study. Note that the Q and R ranges in these figures are not the same, so that differences, if they exist between scales, can be seen more clearly. Here the lines in green and red represent contours in the inertial range, and the lines in blue and black show the contours in the transition and the viscous range, respectively. Based on the spectrum (see Fig. 13 in Appendix B), the cutoff wave numbers corresponding to $\Delta/\eta > 17$ are associated to inertial-range behavior, although clearly it is not exactly a $-5/3$ scaling behavior due to the moderate Reynolds number of the data. The transition range occurs at filter scales such that $\Delta/\eta < 17$.

Consistent with earlier findings [17,18,28,33], the peculiar shape of the joint PDF (tear-drop shape) is seen, qualitatively, at every scale. As seen in Fig. 3, an extended tail appears along the right-Vieillefosse tail and a bulging shape in the $Q > 0$ zone. However, besides many similarities in their shape, we observe that the isocontours tend to broaden at larger scales. In the inertial range
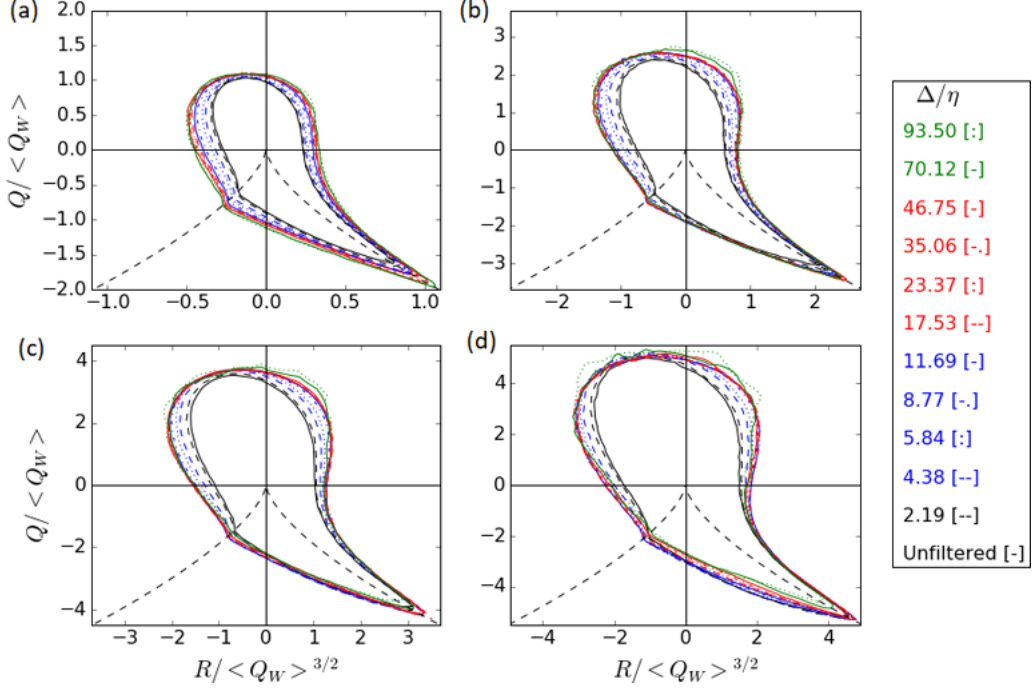
FIG. 3. Isocontours of $\mathcal{P}(Q,R)$ at discrete levels (a) 0.1, (b) 0.01, (c) 0.0032, and (d) 0.001. Different line types and colors represent the contours at various scales Δ/η as indicated in the label at right.

(green and red lines), there is very good collapse, suggesting universal behavior for the velocity gradient tensor at inertial scales. At the smallest filter scale and the unfiltered case (black lines) the contours collapse to different behavior. And the intermediate scales (blue lines) show a rapid change between the two distinct behaviors in the inertial and viscous ranges. As we have seen in Sec. II, the evolution of Q and R is dictated by four distinct mechanisms (RE, PR, VIS, and SGS), but it is not known which is mostly responsible for the differences in joint PDF of Q and R observed at various scales. We defer the detailed analysis of these effects to Sec. IV and for now show further quantities that display "bumps" between the inertial and viscous ranges.

B. Population fraction

As discussed in Sec. II, we divide the Q-R plane in six zones: (1) SFS ($Q > 0$), (2) SFS ($Q < 0$), (3) SNSS, (4) UNSS, (5) UFC ($Q < 0$), and (6) UFC ($Q > 0$). This will enable us to display more clearly the dependence on scale. The population fraction for these zones is defined by integrating the joint PDF in each zone, as $\Pi_{\text{zone}} = \iint_{\text{zone}} \mathcal{P}\, dQ\, dR$. For numerical convenience and better accuracy, we directly count the number of sample points falling in each of the six zones and normalize the sample counts by the global count (1024^3). The population fraction thus obtained in each zone at different scales is shown in Fig. 4 as a function of scale.

Figure 4 shows that the UNSS zone is the most populous zone at the viscous scale, with about 31% of probability for a randomly selected point in the flow to display the UNSS type of topology. In the viscous range, and following in descending order, the next populous zone is SFS ($Q > 0$), which constitutes around 27% of the flow, whereas the least populated zone is found to be the SNSS, which contains only 7% of the total population. On the other hand, the population for each of the remaining zones [UFC ($Q < 0$), UFC ($Q > 0$), SFS ($Q < 0$)] lies between 10% and 12%.

The next very visible conclusion to be reached from the figure is that there are changes towards the inertial range, but noticeably only for two zones: the zone UFC ($Q > 0$) decreases from about
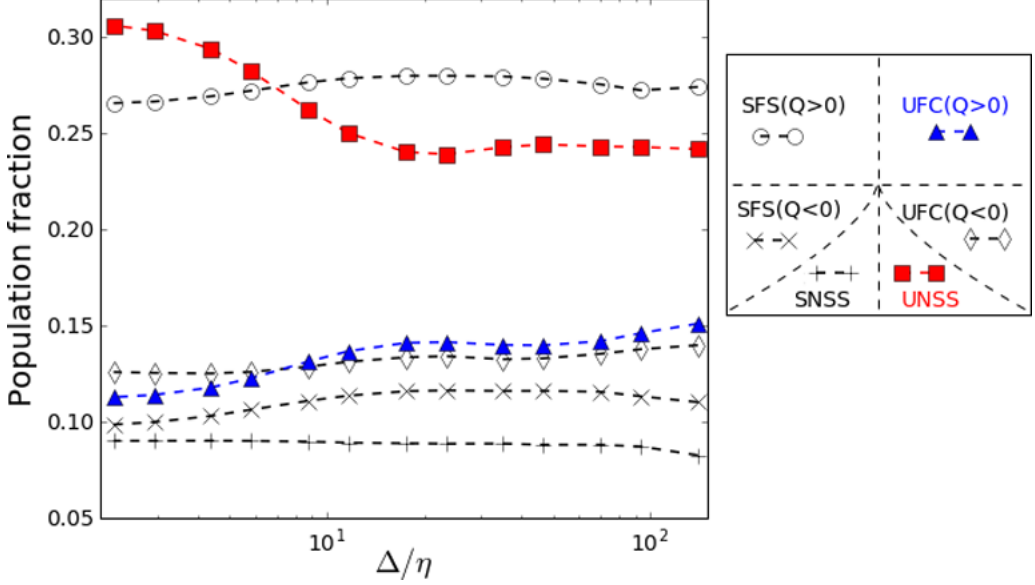
FIG. 4. Population fraction of various local flow topologies as function of filter scale in isotropic turbulence. The symbols associated with each zones are shown in the Q-R plane sketch to the right.

15% to about 11% when going from the inertial to the viscous range. The largest change occurs for the UNSS zone, which has a bump going from 24% in the inertial range up to about 31% in the viscous range. Since the total probability is conserved at each scale, it is evident that a change in population of UNSS, as one goes from an inertial to viscous scale, must be compensated by a change in population in other zones. Zones SFS ($Q < 0$) and UFC ($Q < 0$) show marginal changes in their populations of about 1.5%.

So, overall, the takeaways from the result of population fraction are following: (1) more than half of the total fluid particles at any scale are characterized by UNSS and SFS ($Q > 0$) type topology, (2) no matter what the scale is, the population of SFS ($Q > 0$) remains always constant, and (3) the UNSS topology shows the largest bump in its population going from the inertial to the viscous range.

A change in population in these various zones is expected to indicate a qualitative change in the dynamics of turbulence; for example, the vortex-stretching mechanism can be expected to be different in the inertial and viscous ranges. In order to examine vortex stretching in more detail, we next present the influence of filter scale on the alignment of vorticity and strain-rate eigenvectors.

C. Vorticity–strain-rate alignment

The vortex-stretching phenomenon in turbulence is thought to play an important role in the energy cascade from large to small scale, a defining feature of turbulence. Mathematically, the vortex-stretching term ($\mathcal{V}_\omega$) is expressed as

$$\mathcal{V}_\omega = S_{ij}\omega_i\omega_j, \tag{11}$$

where S_{ij} the is strain-rate tensor and ω_i is the vorticity vector. Expressing $\mathcal{V}_\omega$ in the principal coordinate system of the strain-rate tensor, we can write

$$\mathcal{V}_\omega = \omega^2 \sum_{i=1}^{3} \lambda_i \cos^2(\hat{e}_i, \hat{\omega}), \tag{12}$$
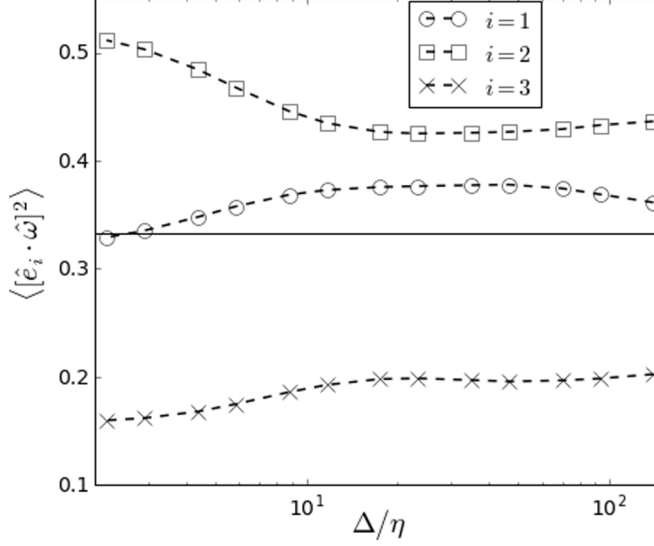
FIG. 5. Average cosine-square of the angle between vorticity vector and the three eigenvectors ($\hat{e}_i$) of a strain-rate tensor. Here $i = 1$, 2, and 3 represent eigenvectors corresponding to the largest, intermediate, and smallest eigenvalues of strain-rate tensor, respectively.

where $\hat{\omega}$ is the unit vorticity vector and λ_i and $\hat{e}_i$ are eigenvalues and eigenvectors of the strain-rate tensor, respectively. The index $i = 1$, 2, and 3 indicates, respectively, the eigenvectors corresponding to the largest, intermediate, and smallest eigenvalues of the strain rate. Though Eq. (12) represents the vortex-stretching term, it can also be seen as the weighted average of strain-rate eigenvalues where the term $\cos^2(\hat{e}_i, \hat{\omega})$ represents the weights associated to each eigenvalue [41]. By definition the term $\cos^2(\hat{e}_i, \hat{\omega})$ represents alignment between the vorticity and the eigenvectors of strain-rate tensor. It should be noted that the alignment between $\hat{\omega}$ and $\hat{e}_i$ can be classified in the following three categories: (1) uniform or random alignment, (2) parallel or biased towards alignment, and (3) biased towards orthogonal alignment. Such categories can be easily identified by evaluating the average value of $\cos^2(\hat{e}_i, \hat{\omega})$, as follows [30,42]: (1) $\langle \cos^2(\hat{e}_i, \hat{\omega}) \rangle = 1/3$ implies random alignment, (2) $\langle \cos^2(\hat{e}_i, \hat{\omega}) \rangle > 1/3$ implies biased alignment, and (3) $\langle \cos^2(\hat{e}_i, \hat{\omega}) \rangle < 1/3$ implies orthogonal alignment.

In Fig. 5 we present the averaged values of $\cos^2(\hat{e}_i, \hat{\omega})$ calculated at various filtering scales. Alignments in the inertial range have been reported in prior studies; e.g., Lozano-Durán *et al.* [33], Tao *et al.* [43,44], and Higgins *et al.* [45] studied these alignments at a fixed scale in the inertial range (measurement limitations did not allow changing the filtering scale). Also, in an interesting recent study, Fiscaletti *et al.* [46,47] reported on alignment of vorticity with filtered strain rates but the latter being at various larger filtering scales. They found that vorticity at small scales tended to align with the stretching direction if the strain rate was filtered at a sufficiently larger scale. Note that in the present study, we keep the same filtering scale and thus limit the analysis to the "self-stretching" mechanism at a fixed scale rather than "interscale stretching."

At the viscous scale (left part of the figure), we confirm prior observations (see Ref. [3] and references therein): for $i = 1$, $\langle \cos^2(\hat{e}_i, \hat{\omega}) \rangle$ is close to 1/3, meaning no preferential alignment of vorticity with the eigenvector corresponding to the largest eigenvector of the strain rate. For $i = 2$, $\langle \cos^2(\hat{e}_i, \hat{\omega}) \rangle$ is larger than 1/3, indicating a strong alignment tendency of vorticity along intermediate eigenvector, and or $i = 3$, $\langle \cos^2(\hat{e}_i, \hat{\omega}) \rangle$ is much smaller than 1/3, implying a bias towards orthogonal alignment with the most contracting strain rate.

However, in the inertial range, we observe a noticeable reduction in the inertial-range vorticity alignment along the inertial range intermediate eigenvector ($i = 2$), while for $i = 1$, we see somewhat

increased propensity of vorticity alignment, although it remains smaller than the alignment with the intermediate strain eigendirection. And, unlike $i = 1$ and 2, the (lack of) alignment for $i = 3$ is almost constant across the scales.

At this point we may connect the tendency of vorticity alignment along $i = 1$ and 2 with the population decrease seen earlier for the UNSS zone (Fig. 4). For UNSS, the two eigenvalues become quite close to each other, and as shown in Ref. [48], the vorticity alignment will be very large along the intermediate eigenvector when the two positive eigenvalues of the strain-rate tensor come close to each other. Thus it makes sense that when the filter size increases, both tendencies are reduced: the fraction of UNSS points and a decrease (but not a disappearance) in the alignment of filtered vorticity with the strain-rate intermediate eigendirection.

We have performed much of the analyses presented in this paper using the other filters (box, Gaussian and spectral cutoff), and qualitatively very similar results can be obtained for the first two types of filters (see Appendix B). The exception is the spectral cutoff filter, for which the behavior of the SGS terms and RE can be markedly different depending on whether the quadratic nonlinearities involved in these terms are dealiased or not. Since dealiasing introduces nonlocality in physical space, the interpretation of these terms in the context of Lagrangian models for the filtered VGT (which depend on the local value of the velocity gradient tensor along a Lagrangian trajectory) becomes more ambiguous. As a result, in this study the use of the Eyink-Aluie filter was adopted.

IV. PROBABILITY EVOLUTION IN Q-R SPACE

In the previous section, differences between the viscous and inertial range behaviors were identified. The observations raise the question whether the observed changes when going from the inertial to the viscous range occur due to inherent changes in the pressure Hessian as a function of scale, or whether the trends can be explained since the viscous term disappears towards the inertial range while being "replaced" by an SGS term that may not entirely resemble the viscous term. Or the situation could be caused by a some particular combination of these different terms. In order to quantify the effects of pressure, viscous, and SGS terms onto the evolution of the velocity gradient invariants Q and R in a statistically robust and meaningful way, one may evaluate these terms effects on the evolution of the joint PDF of Q and R ($\mathcal{P}$). The evolution equation of $\mathcal{P}$ is given by the Fokker-Planck equation [49]:

$$\frac{\partial \mathcal{P}}{\partial t} + \vec{\nabla} \cdot (\mathcal{P}\vec{V}) = 0, \tag{13}$$

where $\vec{\nabla}$ represents gradient operator in the Q-R plane, and $\vec{V}$ is the "velocity" associated with the probability flux $\mathcal{P}\vec{V}$. In the Q-R plane, the "velocity" can be written as

$$\vec{V} = V_R \hat{e}_R + V_Q \hat{e}_Q = \left\langle \frac{dR}{dt} \middle| R, Q \right\rangle \hat{e}_R + \left\langle \frac{dQ}{dt} \middle| R, Q \right\rangle \hat{e}_Q, \tag{14}$$

where V_R and V_Q are the velocity components of $\vec{V}$ along unit vectors $\hat{e}_R$ and $\hat{e}_Q$, respectively. The expressions for V_R and V_Q can be obtained by conditionally averaging the terms that determine the rate of change of Q (7) and R (8), as

$$V_Q = \left\langle \frac{dQ}{dt} \middle| R, Q \right\rangle = \underbrace{-3R}_{V_Q^{\mathrm{RE}}} + \underbrace{\langle A_{ij} H_{ji}^{\mathrm{PR}} | R, Q \rangle}_{V_Q^{\mathrm{PR}}} + \underbrace{\langle A_{ij} H_{ji}^{\mathrm{VIS}} | R, Q \rangle}_{V_Q^{\mathrm{VIS}}} + \underbrace{\langle A_{ij} H_{ji}^{\mathrm{SGS}} | R, Q \rangle}_{V_Q^{\mathrm{SGS}}}, \tag{15}$$

$$V_R = \left\langle \frac{dR}{dt} \middle| R, Q \right\rangle = \underbrace{\frac{2}{3}Q^2}_{V_Q^{\mathrm{RE}}} + \underbrace{\langle A_{ij} A_{jk} H_{ki}^{\mathrm{PR}} | R, Q \rangle}_{V_R^{\mathrm{PR}}} + \underbrace{\langle A_{ij} A_{jk} H_{ki}^{\mathrm{VIS}} | R, Q \rangle}_{V_R^{\mathrm{VIS}}} + \underbrace{\langle A_{ij} A_{jk} H_{ki}^{\mathrm{SGS}} | R, Q \rangle}_{V_R^{\mathrm{SGS}}}, \tag{16}$$

where the conditional averages are evaluated by dividing the R-Q plane into discrete bins.
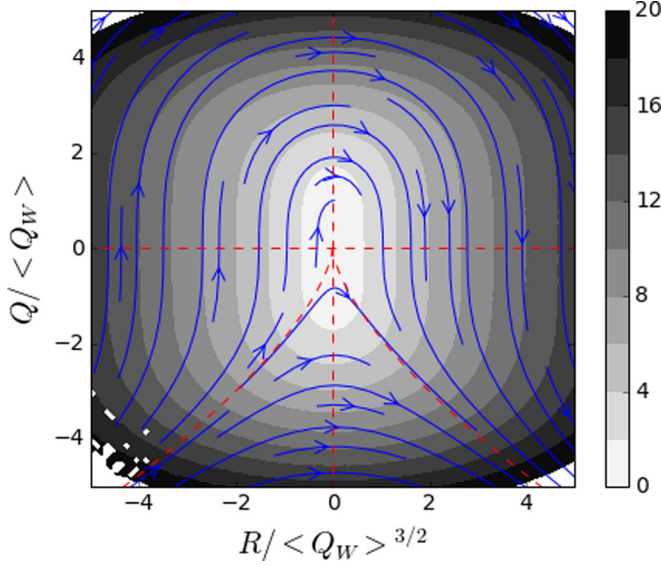
FIG. 6. Streamline plot of $\vec{V}$ for RE effect, i.e., the vector field $(-3R, \frac{2}{3}Q^2)$, which is the same at all scales.

In Eqs. (15) and (16), the velocity components V_Q and V_R can be seen to be composed of four different subterms representing the restricted Euler (RE), deviatoric pressure Hessian (PR), viscous diffusion Hessian (VIS), and the effects of subgrid stress (SGS), respectively. Such a decomposition of V can help us in isolating the role of each of these effects separately, as a function of filter scale Δ.

A. Streamline plots

The RQ velocity field in the plane can be visualized by plotting its streamlines and using contours to show the velocity's magnitude. Such streamline plots have appeared in prior studies of $\mathcal{P}$ [2,17,18,23,33]. While most of these studies focused at the viscous scale, the role of SGS on $\mathcal{P}$ was first considered in Ref. [18], wherein the relevant statistics were obtained by filtering the experimental velocity field at a fixed, experimentally constrained, filter scale. Also, due to the unavailability of a pressure field in the experiments, the result for a deviatoric pressure Hessian could not be reported.

The RQ velocity components required to plot the streamlines are evaluated by conditionally averaging the terms appearing on the right-hand side of Eqs, (15) and (16). The velocity results of Q component (V_Q) are normalized by $\langle Q_W \rangle^{3/2}$ and those of R component (V_R) are normalized by $\langle Q_W \rangle^2$.

In Figs. 6–9, we show the streamlines corresponding to RE, PR, VIS, and SGS terms, respectively, obtained from the fields filtered at scales $\Delta/\eta = 70, 35, 18, 9, 4,$ and 2. The color bar in the figure shows the magnitude of the corresponding RQ velocity field. Note that the RQ velocity from the RE term is deterministic, is the same at any scale, and has been shown many times [3]. It is reproduced here for convenience to display the vector magnitudes and compare with other terms. As pointed out before (Cantwell [2], Ooi *et al.* [17], van der Bos *et al.* [18], Chevillard *et al.* [23]), the RE velocity and streamlines point from the left region of the phase space (including the left-Vieillefosse tail) towards the right region of the phase space (and towards the right-Vieillefosse tail) after circling above the origin in the rotation-dominated region, or going underneath the origin in the strain-dominated region. This occurs along lines of constant invariant $\frac{27}{4}R^2 + Q^3$ irrespective of scale. In the absence of PR, VIS, and SGS effects, the dynamics approach the right-Vieillefosse tail and lead to finite-time singularity [2]. In DNS and at viscous scale, the effects of PR and VIS are large enough and can oppose the RE effects so that a stationary joint PDF with the tear-drop shape is achieved.
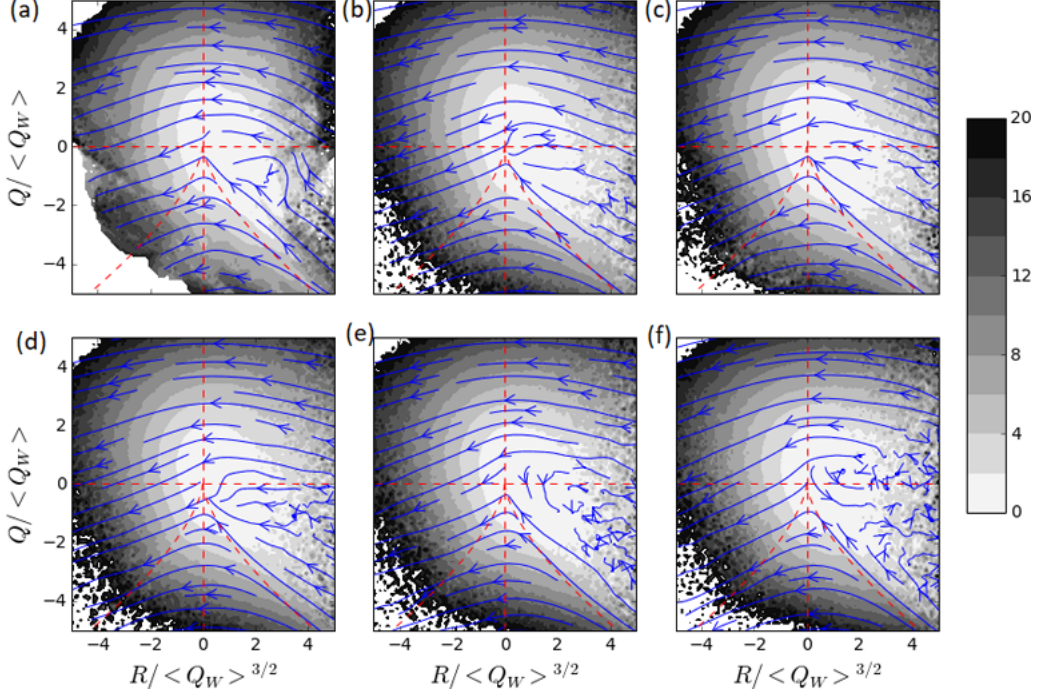
FIG. 7. Streamline plot for $\vec{V}$ for the PR effect at scales $\Delta/\eta =$ (a) 70, (b) 35, (c) 18, (d) 9, (e) 4, and (f) 2.

In Fig. 7, the streamlines corresponding to the deviatoric pressure Hessian at different scales are shown. Unlike RE, the streamlines for PR move from right to left, opposing the RE trends along the right-Vieillefosse tail region. The PR velocity magnitudes are comparable to those of RE and interestingly do not appear to depend strongly on scale. Thus, the PR term opposes RE not only at the viscous scale but also throughout the inertial range. However, some differences in streamline patterns can be observed. At viscous scales in the UFC ($Q < 0$) zone, the streamlines reverse direction and stay within this zone only [Figs. 7(e) and 7(f)], whereas in the inertial range the streamlines cover the Q-R plane more uniformly, overall going from right to left.

Next, we present streamlines for the viscous RQ velocity in Fig. 8. Unlike RE and PR, and as observed in prior analyses [18,23], we observe that the streamlines are directed toward the origin over the entire Q-R plane. The magnitude of these terms can be estimated using Kolmogorov scaling arguments [18], leading to $(\Delta/\eta)^{-4/3}$ so that the magnitude keeps increasing as we move from inertial to viscous scales. Although the magnitudes appear to be negligibly small at the largest scale [Fig. 8(a)], the streamlines are still well defined and well converged. Comparing the viscous streamlines with those of RE, we note that the viscous effects favor the RE trends in zones SFS ($Q > 0$) and SNSS and oppose it in zones UFC ($Q < 0$) and UNSS. The latter trend means that the viscous effect acts alongside the deviatoric pressure Hessian in opposing the RE effect along the right-Vieillefosse tail, thus, helping to counteract the RE finite-time singularity.

In Fig. 9 we show the velocity magnitude and streamlines for the SGS term. As expected, this velocity field's magnitudes are larger at inertial scales and become smaller at viscous scales. Moreover, we also observe a significant difference in the direction of streamlines between inertial and viscous scales. On the right-half plane in inertial range [Figs. 9(a)–9(c)], the SGS is seen to be pushing its streamlines upward in such a way that they directly oppose the RE effect over the complete right-half plane, i.e., for any $R > 0$. But in the viscous range, in the $R > 0$, $Q > 0$ quadrant, the SGS term has a small magnitude and ill-defined direction. So, while SGS
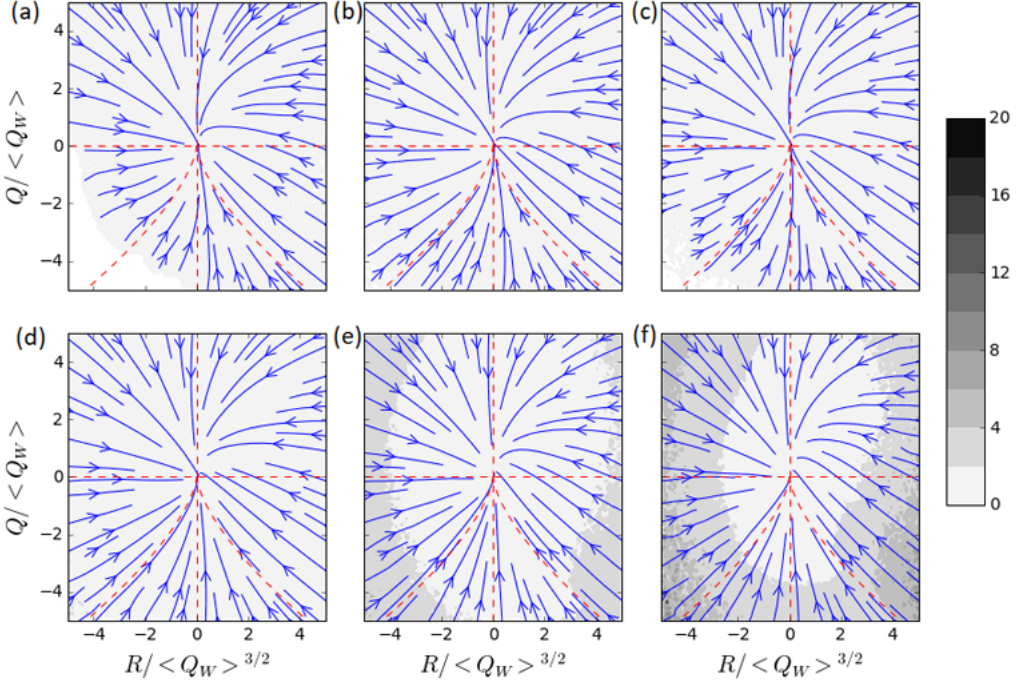
FIG. 8. Streamline plot $\vec{V}$ for the VIS effect at scales, $\Delta/\eta =$ (a) 70, (b) 35, (c) 18, (d) 9, (e) 4, and (f) 2.

terms oppose the RE trends along the right-Vieillefosse tail and in the $Q > 0$ upper plane in the inertial range, in the viscous range this opposing effect is restricted to the right-Vieillefosse tail region.

Thus, in the inertial range SGS combine with Hessian and viscous effects to help prevent the occurrence of the RE-induced finite-time singularity. On the other hand, the streamlines for SGS on the left-half plane $R < 0$ point in a direction that appears generally perpendicular to the RE trends. So it does not directly oppose the RE behavior in the three $R < 0$ regions. Comparing the streamlines of PR and SGS at inertial and viscous scales, we find them to be slightly different in the UFC lower and upper zones, respectively, whereas the streamlines for viscous effects have been found to be fairly independent of scales in any of the zones.

Our main objective for this analysis has been to elucidate which terms are responsible for the "change" in statistics when going from the inertial to the viscous range. To distill such a conclusion from an entire vector plot for various scales is challenging given the complexity of the trends summarized above. A more compact diagnostics of the net effects of each of the terms as a function of scale is required. In the next subsection, an attempt is made to define such a diagnostic based on net fluxes of probability density in RQ phase space.

B. Flux measurements

To compactly quantify the effects of the RE, PR, VIS, and SGS terms, in this section we present results for the total probability flux, as calculated across a closed boundary placed in the Q-R plane. We choose a circle centered at the origin as shown in Fig. 10. We ask what is the flux of probability density corresponding to each of the terms. The total (integrated) flux crossing the circle can be obtained by

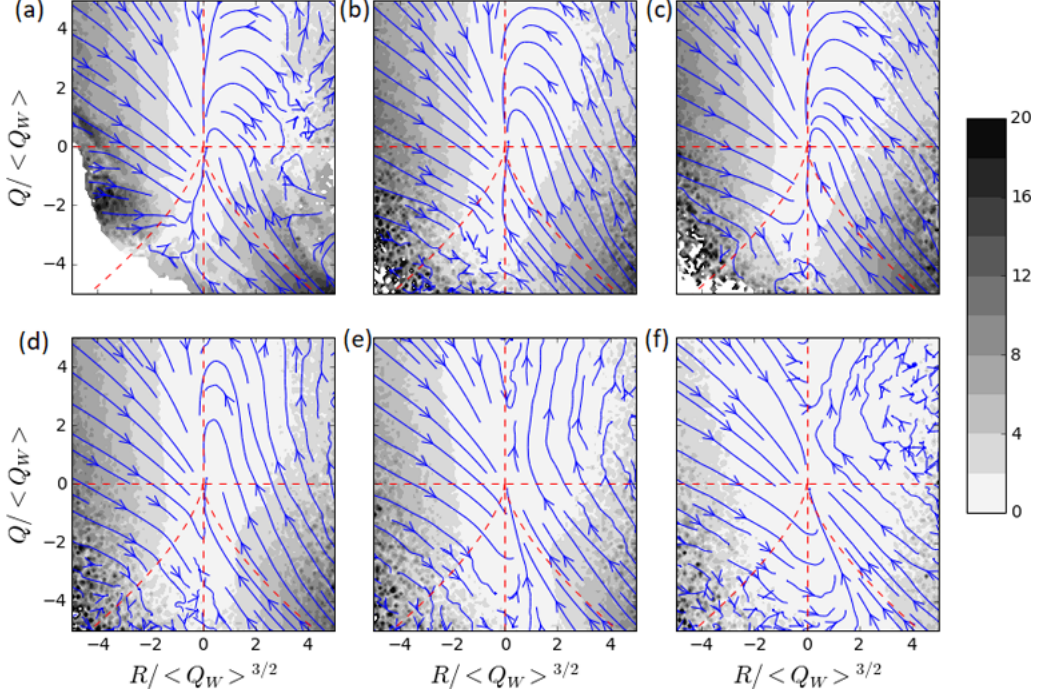$$J = \oint_c (\mathcal{P}\vec{V} \cdot \hat{n})dS, \tag{17}$$

FIG. 9. Streamline plot for $\vec{V}$ for the SGS effect at scales, $\Delta/\eta =$ (a) 70, (b) 35, (c) 18, (d) 9, (e) 4, and (f) 2.

where c is the closed surface (circle), $\hat{n}$ is the normal vector (outward) on the surface, dS is differential surface (circle length) along c, and J represents the total flux of probability density.

Note that in order to measure J it is convenient to replace the surface integral by a sum over all points inside the circle. Using the divergence formula, we write

$$J = \iint \vec{\nabla} \cdot (\mathcal{P}\vec{V}) dQ\, dR = J_{\text{RE}} + J_{\text{PR}} + J_{\text{VIS}} + J_{\text{SGS}}, \qquad (18)$$

where J_{RE}, J_{PR}, J_{VIS}, and J_{SGS} are fluxes due to the divergences of $\mathcal{P}\vec{V}_{\text{RE}}$, $\mathcal{P}\vec{V}_{\text{PR}}$, $\mathcal{P}\vec{V}_{\text{VIS}}$, and $\mathcal{P}\vec{V}_{\text{SGS}}$, respectively. The statistically stationary condition in the Fokker-Planck equation (13) implies that these contributions must balance:

$$J_{\text{RE}} + J_{\text{PR}} + J_{\text{VIS}} + J_{\text{SGS}} = 0. \qquad (19)$$

Thus some of the terms will be positive, and some will be negative. For example, for the RE term, while the term's velocity is symmetric, the net flux is expected to be outwards since $\mathcal{P}(R, Q)$ is larger along the right Vieillefosse tail than on the left. Hence we will find that RE term causes a net "outward" trend towards singular behavior. This will be denoted as a "sourcelike" behavior. The opposite can be expected for the viscous and SGS terms which correspond to a "sink"-like behavior, with mostly inward pointing flow of probability.

The flux is calculated numerically within the circle on the discrete RQ plane, which is gridded with square mesh of size 0.05 in the dimensionless units for this analysis. The vector fields are sufficiently smooth so that results (not shown) are independent on the grids used to discretize the RQ plane. The results do depend quite strongly on the circle's radius as obviously the probability decreases rapidly with increasing radius. In order to define a diagnostic that is somewhat insensitive
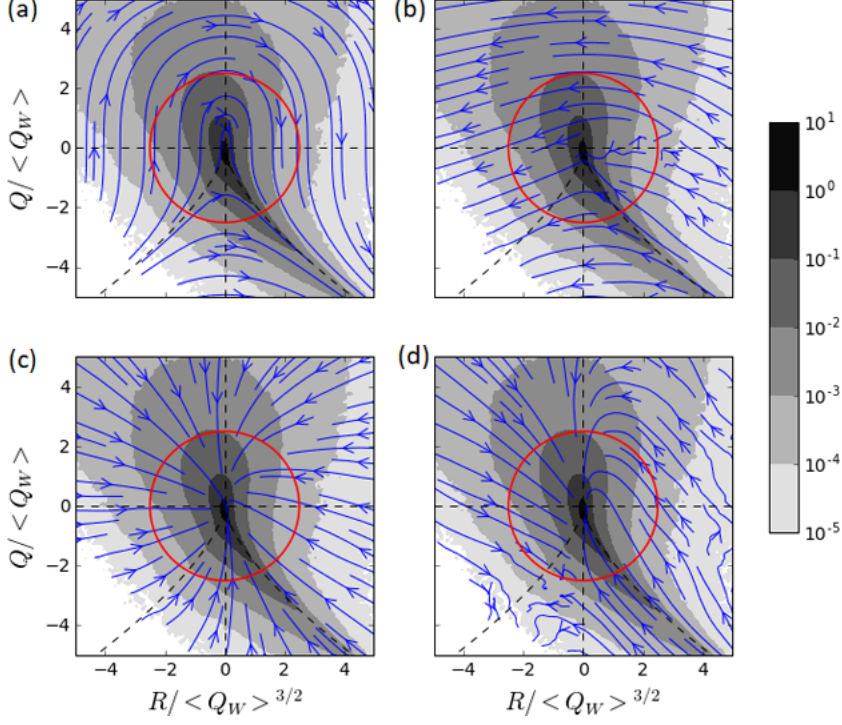
FIG. 10. Representative circle with radius equal to 2.5 centered at the origin of the Q-R plane, shown together with the streamlines for the (a) RE, (b) PR, (c) VIS, and (d) SGS terms. The contour plot indicates the joint PDF $\mathcal{P}(R, Q)$.

to the circle the fluxes are normalized as follows:

$$J_{\text{RE}}^* = \frac{J_{\text{RE}}}{\sqrt{J_{\text{RE}}^2 + J_{\text{PR}}^2 + J_{\text{VIS}}^2 + J_{\text{SGS}}^2}}, \quad J_{\text{PR}}^* = \frac{J_{\text{PR}}}{\sqrt{J_{\text{RE}}^2 + J_{\text{PR}}^2 + J_{\text{VIS}}^2 + J_{\text{SGS}}^2}},$$

$$J_{\text{VIS}}^* = \frac{J_{\text{VIS}}}{\sqrt{J_{\text{RE}}^2 + J_{\text{PR}}^2 + J_{\text{VIS}}^2 + J_{\text{SGS}}^2}}, \quad J_{\text{SGS}}^* = \frac{J_{\text{SGS}}}{\sqrt{J_{\text{RE}}^2 + J_{\text{PR}}^2 + J_{\text{VIS}}^2 + J_{\text{SGS}}^2}}. \tag{20}$$

As a result of this normalization, their magnitude lies between 0 and 1, while the sum of these terms still vanishes. In Fig. 11 we present the normalized flux for each term as function of scale Δ/η, using two radii, 2.5 and 3.25, in the dimensionless RQ units. Comparing the results shown in Figs. 11(a) and 11(b), they appear quite independent of radius in the range [2.5, 3.25].

Now comparing the different terms in Fig. 11, as expected the RE term (red line) is positive, i.e., it acts as a "source." Conversely, and consistent with the streamline plots for the VIS and SGS terms [Figs. 10(c) and 10(d)], we find that the total integrated fluxes for the viscous and SGS terms are negative and dependent on scale (black and blue lines in Fig. 11). As expected, the viscous term at small scales acts as a sink, and its magnitude decreases with increasing scale, becoming very small in the inertial range. We note that the viscous flux actually scales as $(\Delta/\eta)^{-4/3}$ in the inertial range (see Fig. 12, which plots only the viscous term in log-log axes to highlight the scaling), consistent with what has been reported earlier by Bos *et al.* [18]. The SGS term displays the opposite behavior. Its strength is small in the viscous range, but subsequently grows and achieves a constant value (due to the normalization) in the inertial range.
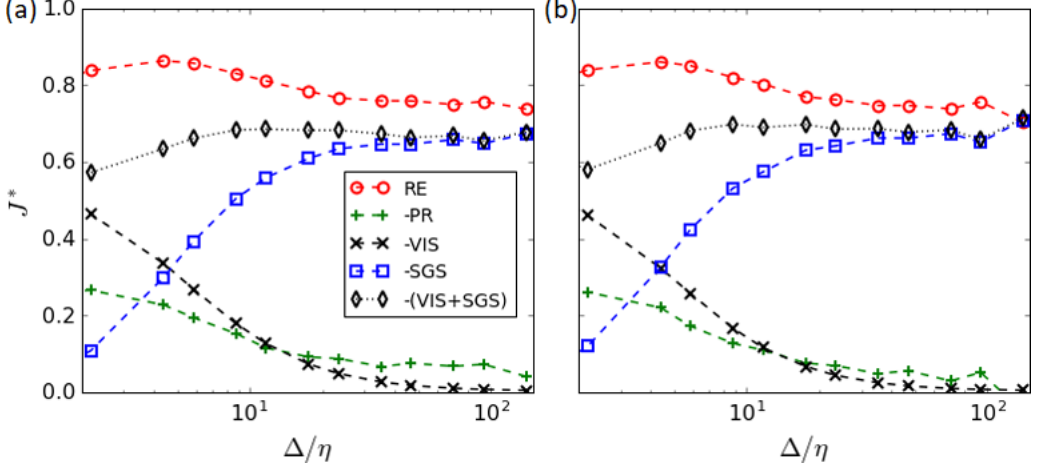
FIG. 11. Normalized fluxes for the RE, PR, VIS, and SGS terms across circles as function of filter scale Δ/η, with radii (a) $r = 2.5$ and (b) $r = 3.25$ units. Note that the RE term (red) is positive, while PR, VIS, and SGS terms are negative and are shown with opposite sign. The sum of all contributions equals 0 by construction.

The flux for the pressure (PR) term is shown with the green line in Fig. 11. It is in fact rather small, but this is due to cancellations stemming from large negative contributions along the right-Vieillefosse tail opposing RE, but this is mostly canceled by large positive contributions in the upper left quadrant of the RQ plane, where there is significant probability and the PR term points away from the origin towards a negative R direction. Still, overall the PR term is negative, i.e., it opposes the formation of singularities.

The black rhombus shows the SGS and VIS flux terms added. It appears that when decreasing scale from the inertial range and approaching the viscous range, the SGS term decreases slightly more rapidly than what the VIS term manages to grow. As a result the PR term must increase
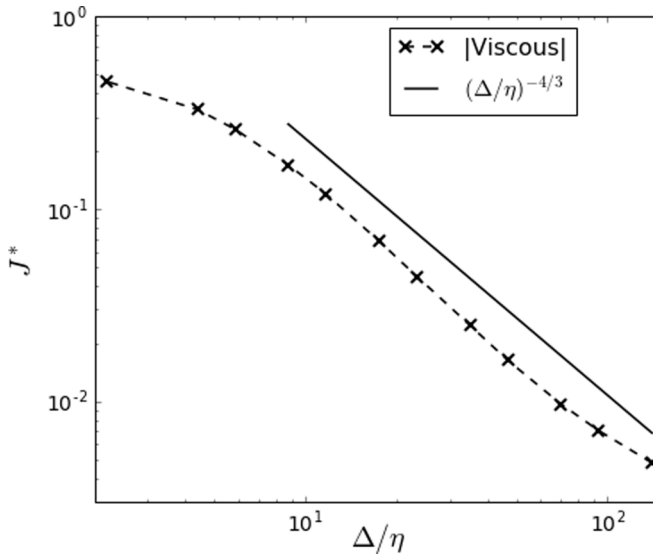

FIG. 12. Power law for VIS effects.

to make up for the difference and establish stationary statistics. Finally, all three terms, VIS, SGS, and PR display different behavior when transitioning between the inertial and viscous ranges.

V. CONCLUSIONS

In this paper, we have studied the dynamics of the filtered velocity gradient tensor in terms of its invariants Q and R with an emphasis on length scales including the viscous and inertial ranges. For this purpose, we have employed a DNS dataset of isotropic turbulence at a Taylor microscale Reynolds number of 433, and the Eyink-Aluie filter [35] has been used to obtain a filtered field at various scales, ranging from inertial to viscous scales.

The main emphasis has been to establish whether the change between inertial and viscous ranges that is known to occur for the derivative skewness can also be observed for statistics pertaining to other properties of the (filtered) VGT such as Q and R. For this purpose in Sec. III, we have presented results for the joint PDF of Q and R, the population fraction of the six Q-R plane zones, and the averaged value of the cosine-squares of the angle between vorticity and eigenvectors of strain-rate tensor.

Based on the results shown in Figs. 3–5, we list the major findings as follows:

(1) The well-known tear-drop shape of $\mathcal{P}(Q, R)$ occurs at every scale considered in our analysis. Such observations are consistent with earlier works of van der Bos *et al.* [18], Chertkov *et al.* [24], Borue and Orszag [28], and Lozano-Durán *et al.* [33].

(2) Through the isoprobability contours of $\mathcal{P}$ (Fig. 3), we have demonstrated that, even while displaying qualitatively the tear-drop shape, their details depend on scale in the transition region between the viscous and inertial range. In the inertial range, results collapse quite well consistent with scale independence of $\mathcal{P}$ in the inertial range (note that at the resolution and Reynolds numbers, small trends due to intermittency cannot be ruled out, however).

(3) The alignment of vorticity and strain-rate eigenvectors (Fig. 5) and some of the population fractions of the various Q-R plane zones [Fig. 4, specifically the UNSS and UFC ($Q > 0$) flow topologies] also display an inertial-viscous transition "bumps," akin to that of the derivative skewness factor. The UNSS topology is known to be the topology most correlated to dissipation of kinetic energy. Our observation that the UNSS topology has the clearest bump behavior supports the view that the small scales in turbulence adjust their structure so as to increase the efficiency at which they are able to dissipate kinetic energy.

In an attempt to pinpoint the dynamical reason for the quantitative changes between the viscous and inertial ranges, we consider the different mechanisms that govern the evolution of the joint PDF of Q and R at various scales. Such mechanisms (restricted Euler, deviatoric pressure Hessian, viscous diffusion Hessian, and subgrid Hessian terms) can be examined in a statistically robust fashion using conditional averages in the probability evolution (Figs. 6–9) and net flux towards or away from the origin as simple measure for "singularity-generating" or "singularity prevention" trends. From these results, one may conclude that the lack of constancy of the SGS + VIS flux as function of scale (a slight decrease in magnitude) appears to be due to a more rapid decrease in SGS than what VIS manages to increase towards the viscous range. Since the VIS term was shown to follow the expected $-4/3$ power-law scaling in the inertial range, the "anomalous" behavior may be more associated with the SGS term, wjocj appears to decrease rapidly towards the viscous range, before VIS can make up the difference. The PR term must increase at decreasing scale to make up for the difference.

Hence, it appears that in models for filtered VGT in which PR, VIS, and SGS terms must all be modeled, different approaches may be required for each of the three terms in the inertial and in the viscous ranges, even if in practice recent results suggest that to some approximation treating the VIS and SGS similarly yields acceptable results. Finally, we remark that the observed bump phenomena could also be linked to activity of small-scale coherent structures, a question that the statistical analysis used here does not directly address.

APPENDIX A: SCISERVER PLATFORM

The SciServer is an online analysis platform which has been recently added alongside the Johns Hopkins Turbulence Database (JHTDB). The JHTDB contains several DNS databases, like forced isotropic turbulence, magnetohydrodynamics, channel flow, and buoyancy-driven turbulence. Access to these datasets is facilitated through various functions such as *GetPosition, GetVelocityGradient, GetPressureHessian,* etc., written in Fortran, C, and MATLAB. Over the past few years, the JHTDB has been used in wide range of turbulence studies involving velocity gradients, pressure Hessian, etc. [39,50–54]. While the present JHTDB functions obtain gradients in physical space using the finite difference method, a more accurate way is to use the fast Fourier transform (FFT). FFT can also be used in filtering the velocity fields at various scales. However, due to its nonlocal nature Fourier transformations require whole 3D field to be downloaded on the user's computer, which heavily depends on the network connectivity of the user's computer with the JHTDB. To avoid such bottlenecks and to enable FFT computations "near" the JHTDB the SciServer platform is directly connected to JHTDB through a 10 Gigabit ethernet connection. SciServer provides docker containers with the relevant libraries installed and Jupyter notebooks. More information about SciServer can be found at http://www.sciserver.org.

APPENDIX B: THE EYINK-ALUIE FILTER AND ITS COMPARISON WITH OTHER FILTERS

The purpose of filtering a DNS field is to separate scales which are larger than a given cutoff scale Δ, where Δ is the filter width used. An intuitive way of filtering is to perform it in Fourier space, as

$$\widehat{\widetilde{u}_1} = \mathcal{F}\{\widetilde{u}_1\} = \hat{G}(\kappa)\hat{u}_1(\kappa), \tag{B1}$$

where $\mathcal{F}$ is the Fourier operator, and the quantity with s hat [$\hat{\,}$] represents the Fourier transform of the field. Though several types of filters exist, the most commonly used filters in the turbulence literature have been sharp-spectral, top-hat (box), and Gaussian. For these filters, the function G in Fourier space is given by [34]

$$\widehat{G}(\kappa) = \begin{cases} \mathcal{H}(\kappa_c - |\kappa|): & \text{Sharp-spectral} \\ \sin(0.5\kappa\,\Delta)/(0.5\kappa\,\Delta): & \text{Top-hat (box)} \\ \exp(-\kappa^2\Delta^2/24): & \text{Gaussian} \end{cases}, \tag{B2}$$

where $\mathcal{H}$ is the Heaviside function, κ represents wave number, and Δ is the filter width which is related to cutoff wave number κ_c by

$$\kappa_c = \frac{\pi}{\Delta}. \tag{B3}$$

In practice desirable properties of filters are the following [35]:
  (i) G must be positive in physical space.
  (ii) G to be infinitely differentiable with its Fourier transform $\widehat{G}$ to be positive and compactly supported inside the ball of radius 1.
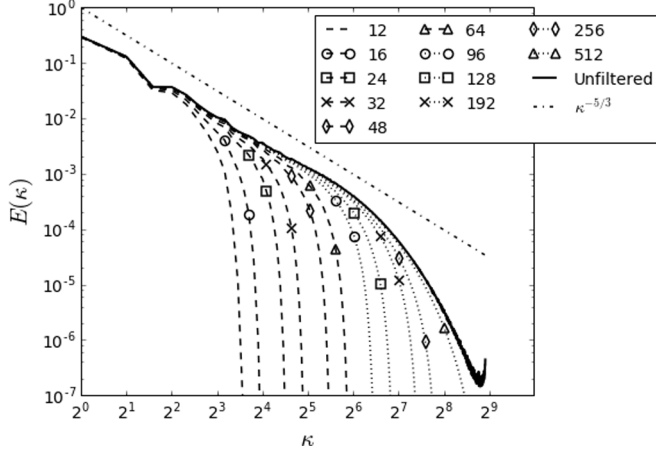
FIG. 13. Energy spectra obtained from fields which are filtered using the Eyink-Aluie filter at various filter wave numbers defined as $\kappa_c = \pi/\Delta$.

Beside these two desirable properties, a filter must also be normalized so that $\int G(r)dr = 1$, which means $\widehat{G}(0) = 1$.

To construct a filter with all the above properties, Eyink and Aluie [35] started with a filter function G_0 whose Fourier transform ($\widehat{G}_0$) remains compactly supported inside the ball of radius 1, as

$$\widehat{G}_0(\kappa) = \begin{cases} \exp\left(-\frac{\kappa^2}{1/4-\kappa^2}\right), & \text{if } |\kappa| < 1/2, \\ 0, & \text{otherwise.} \end{cases} \tag{B4}$$

Subsequently, the positivity of G_0 in physical space can be checked by taking the inverse Fourier transform of $\widehat{G}_0$ (B4) as

$$G_0(r) = \frac{1}{2\pi} \int \widehat{G}_0(\kappa)\cos(kr)d\kappa. \tag{B5}$$

In this equation, it is easy to see that the function G_0 is not positive everywhere because of the cosine term sitting in Eq. (B5). Therefore, to make it positive, Eyink and Aluie [35] took the square of G_0:

$$G(r) = [G_0(r)]^2. \tag{B6}$$

The Fourier transform of G (B6) can be obtained easily by the convolution theorem, as

$$\widehat{G}(\kappa) = \frac{1}{2\pi} \int \widehat{G}_0(p)\widehat{G}_0(\kappa - p)dp. \tag{B7}$$

Thus, Eq. (B7) completes the construction of Eyink-Aluie filter in one dimension, which is ensured to satisfy all the required properties. 3D versions are built using tensor products.

To exhibit the effects of the Eyink-Aluie filter on turbulence spectra, in Fig. 13, we present the energy spectra obtained from the unfiltered field (DNS) and the fields filtered using Eyink-Aluie filter at various filter wave numbers. As can be seen, the spectral decay is quite rapid, showing very good spectral localization even if no negative lobes of the filter occur in physical space.

Finally, as a sample of our analysis using other filters, in Fig. 14 the population fraction of UNSS topology is shown as a function of Δ/η. Here, at small scales, all the filters predict almost the same population. However, at large scales, the box filter shows a monotonous increase in population, as one goes from large scale to small scale, whereas the sharp and Eyink-Aluie filters predict almost constant population from the large to the inertia scales. Although the sharp and Eyink-Aluie filters' results exhibit similar behavior, the numerical values are different. On the other hand, the Gaussian
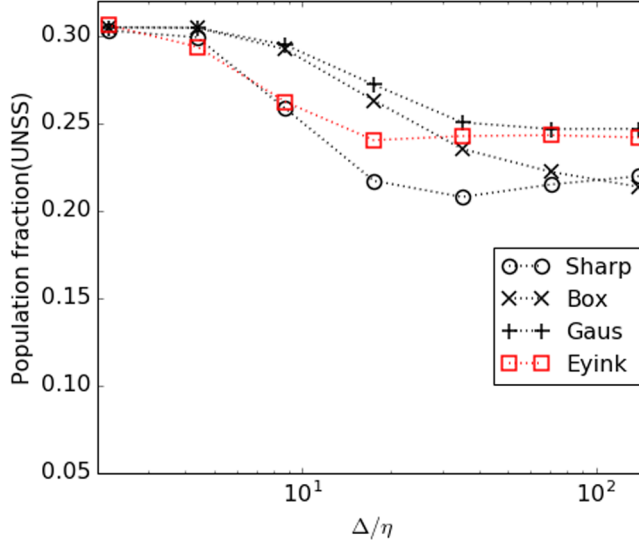
FIG. 14. Population fraction of the UNSS zone as a function of Δ/η obtained from spectral cutoff (circles), top-hat (crosses), Gaussian (plus), and Eyink filters (red squares).

filter shows also the constant population; however, the jump in population seems to appear a bit before than what has been observed for sharp and Eyink-Aluie filters, as expected for different compactness properties.

Note that the size Δ of the filter is associated here to the cutoff wave number using the usual definition $\Delta = \pi/\kappa_c$. A larger filter scale results if the definition in terms of the second moment [34] of the filter is used.

[1] M. S. Chong, A. E. Perry, and B. J. Cantwell, A general classification of three-dimensional flow fields, Phys. Fluids A **2**, 765 (1990).

[2] B. J. Cantwell, Exact solution of a restricted Euler equation for the velocity gradient tensor, Phys. Fluids A **4**, 782 (1992).

[3] C. Meneveau, Lagrangian dynamics and models of the velocity gradient tensor in turbulent flows, Annu. Rev. Fluid Mech. **43**, 219 (2011).

[4] J. Jiménez, A. A. Wray, P. G. Saffman, and R. S. Rogallo, The structure of intense vorticity in isotropic turbulence, J. Fluid Mech. **255**, 65 (1993).

[5] J. Jiménez and A. A. Wray, On the characteristics of vortex filaments in isotropic turbulence, J. Fluid Mech. **373**, 255 (1998).

[6] I. Hosokawa, S.-I. Oide, and K. Yamamoto, Existence and significance of soft worms in isotropic turbulence, J. Phys. Soc. Jpn. **66**, 2961 (1997).

[7] G. Falkovich, K. Gawedzki, and M. Vergassola, Particles and fields in fluid turbulence, Rev. Mod. Phys. **73**, 913 (2001).

[8] F. Toschi and E. Bodenschatz, Lagrangian properties of particles in turbulence, Annu. Rev. Fluid Mech. **41**, 375 (2009).

[9] L. Biferale, A. Scagliarini, F. Toschi, and I. C. for Turbulence Research, On the measurement of vortex filament lifetime statistics in turbulence, Phys. Fluids **22**, 065101 (2010).

[10] R. Maniero, O. Masbernat, E. Climent, and F. Risso, Modeling and simulation of inertial drop break-up in a turbulent pipe flow downstream of a restriction, Int. J. Multiphas. Flow **42**, 1 (2012).

[11] L. Biferale, C. Meneveau, and R. Verzicco, Deformation statistics of sub-Kolmogorov-scale ellipsoidal neutrally buoyant drops in isotropic turbulence, J. Fluid Mech. **754**, 184 (2014).

[12] E. Balkovsky, A. Fouxon, and V. Lebedev, Turbulent Dynamics of Polymer Solutions, Phys. Rev. Lett. **84**, 4765 (2000).

[13] F. Bagheri, D. Mitra, P. Perlekar, and L. Brandt, Statistics of polymer extensions in turbulent channel flow, Phys. Rev. E **86**, 056314 (2012).

[14] G. K. Batchelor, Mass transfer from small particles suspended in turbulent fluid, J. Fluid Mech. **98**, 609 (1980).

[15] S. Parsa, E. Calzavarini, F. Toschi, and G. A. Voth, Rotation Rate of Rods in Turbulent Fluid Flow, Phys. Rev. Lett. **109**, 134501 (2012).

[16] L. Chevillard and C. Meneveau, Orientation dynamics of small, triaxial–ellipsoidal particles in isotropic turbulence, J. Fluid Mech. **737**, 571 (2013).

[17] A. Ooi, J. Martin, J. Soria, and M. Chong, A study of the evolution and characteristics of the invariants of the velocity-gradient tensor in isotropic turbulence, J. Fluid Mech. **381**, 141 (1999).

[18] F. van der Bos, B. Tao, C. Meneveau, and J. Katz, Effects of small-scale turbulent motions on the filtered velocity gradient tensor as deduced from holographic particle image velocimetry measurements, Phys. Fluids **14**, 2456 (2002).

[19] S. Suman and S. S. Girimaji, Velocity gradient invariants and local flow-field topology in compressible turbulence, J. Turbul. **11**, N2 (2010).

[20] M. Danish, S. Suman, and S. S. Girimaji, Influence of flow topology and dilatation on scalar mixing in compressible turbulence, J. Fluid Mech. **793**, 633 (2016).

[21] S. S. Girimaji and S. B. Pope, Material-element deformation in isotropic turbulence, J. Fluid Mech. **220**, 427 (1990).

[22] L. Chevillard and C. Meneveau, Lagrangian Dynamics and Statistical Geometric Structure of Turbulence, Phys. Rev. Lett. **97**, 174501 (2006).

[23] L. Chevillard, C. Meneveau, L. Biferale, and F. Toschi, Modeling the pressure Hessian and viscous Laplacian in turbulence: Comparisons with direct numerical simulation and implications on velocity gradient dynamics, Phys. Fluids **20**, 101504 (2008).

[24] M. Chertkov, A. Pumir, and B. I. Shraiman, Lagrangian tetrad dynamics and the phenomenology of turbulence, Phys. Fluids **11**, 2394 (1999).

[25] S. Suman and S. S. Girimaji, Homogenized Euler equation: a model for compressible velocity gradient dynamics, J. Fluid Mech. **620**, 177 (2009).

[26] S. Suman and S. S. Girimaji, Dynamical model for velocity-gradient evolution in compressible turbulence, J. Fluid Mech. **683**, 289 (2011).

[27] M. Danish, S. Suman, and B. Srinivasan, A direct numerical simulation-based investigation and modeling of pressure Hessian effects on compressible velocity gradient dynamics, Phys. Fluids **26**, 126103 (2014).

[28] V. Borue and S. A. Orszag, Local energy flux and subgrid-scale statistics in three-dimensional turbulence, J. Fluid Mech. **366**, 1 (1998).

[29] A. Pumir, B. I. Shraiman, and M. Chertkov, Geometry of Lagrangian Dispersion in Turbulence, Phys. Rev. Lett. **85**, 5324 (2000).

[30] H. Xu, A. Pumir, and E. Bodenschatz, The pirouette effect in turbulent flows, Nat. Phys. **7**, 709 (2011).

[31] P. L. Johnson and C. Meneveau, Turbulence intermittency in a multiple-time-scale Navier-Stokes-based reduced model, Phys. Rev. Fluids **2**, 072601 (2017).

[32] S. Cerutti, C. Meneveau, and O. M. Knio, Spectral and hyper eddy viscosity in high-Reynolds-number turbulence, J. Fluid Mech. **421**, 307 (2000).

[33] A. Lozano-Durán, M. Holzner, and J. Jiménez, Multiscale analysis of the topological invariants in the logarithmic region of turbulent channels at a friction Reynolds number of 932, J. Fluid Mech. **803**, 356 (2016).

[34] S. B. Pope, *Turbulent Flows* (Cambridge University Press, Cambridge, UK, 2000).

[35] G. L. Eyink and H. Aluie, Localness of energy cascade in hydrodynamic turbulence. I. Smooth coarse graining, Phys. Fluids **21**, 115107 (2009).

[36] N. S. Vaghefi and C. K. Madnia, Local flow topology and velocity gradient invariants in compressible turbulent mixing layer, J. Fluid Mech. **774**, 67 (2015).

[37] M. Danish, S. S. Sinha, and B. Srinivasan, Influence of compressibility on the Lagrangian statistics of vorticity–strain-rate interactions, Phys. Rev. E **94**, 013101 (2016).

[38] N. Parashar, S. S. Sinha, M. Danish, and B. Srinivasan, Lagrangian investigations of vorticity dynamics in compressible turbulence, Phys. Fluids **29**, 105110 (2017).

[39] Y. Li, E. Perlman, M. Wan, Y. Yang, C. Meneveau, R. Burns, S. Chen, A. Szalay, and G. Eyink, A public turbulence database cluster and applications to study Lagrangian evolution of velocity increments in turbulence, J. Turbul. **9**, N31 (2008).

[40] L. Chevillard, S. Roux, E. Lévêque, N. Mordant, J.-F. Pinton, and A. Arnéodo, Lagrangian Velocity Statistics in Turbulent Flows: Effects of Dissipation, Phys. Rev. Lett. **91**, 214502 (2003).

[41] P. L. Johnson and C. Meneveau, Large-deviation statistics of vorticity stretching in isotropic turbulence, Phys. Rev. E **93**, 033118 (2016).

[42] L. Chevillard and C. Meneveau, Lagrangian time correlations of vorticity alignments in isotropic turbulence: Observations and model predictions, Phys. Fluids **23**, 101704 (2011).

[43] B. Tao, J. Katz, and C. Meneveau, Geometry and scale relationships in high Reynolds number turbulence determined from three-dimensional holographic velocimetry, Phys. Fluids **12**, 941 (2000).

[44] B. Tao, J. Katz, and C. Meneveau, Statistical geometry of subgrid-scale stresses determined from holographic particle image velocimetry measurements, J. Fluid Mech. **457**, 35 (2002).

[45] C. W. Higgins, M. B. Parlange, and C. Meneveau, Alignment trends of velocity gradients and subgrid-scale fluxes in the turbulent atmospheric boundary layer, Boundary-Layer Meteorol. **109**, 59 (2003).

[46] D. Fiscaletti, A. Attili, F. Bisetti, and G. E. Elsinga, Scale interactions in a mixing layer—The role of the large-scale gradients, J. Fluid Mech. **791**, 154 (2016).

[47] D. Fiscaletti, G. Elsinga, A. Attili, F. Bisetti, and O. Buxton, Scale dependence of the alignment between strain rate and rotation in turbulent shear flow, Phys. Rev. Fluids **1**, 064405 (2016).

[48] K. K. Nomura and G. K. Post, The structure and dynamics of vorticity and rate of strain in incompressible homogeneous turbulence, J. Fluid Mech. **377**, 65 (1998).

[49] H. Risken, *The Fokker-Planck Equation*, Springer Series in Synergetics Vol. 18 (Springer, Berlin, 1984).

[50] H. Yu, K. Kanov, E. Perlman, J. Graham, E. Frederix, R. Burns, A. Szalay, G. Eyink, and C. Meneveau, Studying Lagrangian dynamics of turbulence using on-demand fluid particle tracking in a public turbulence database, J. Turbul. **13**, N12 (2012).

[51] Y. Li, L. Chevillard, G. Eyink, and C. Meneveau, Matrix exponential-based closures for the turbulent subgrid-scale stress tensor, Phys. Rev. E **79**, 016305 (2009).

[52] H. Yu and C. Meneveau, Scaling of conditional Lagrangian time correlation functions of velocity and pressure gradient magnitudes in isotropic turbulence, Flow Turbul. Combust. **85**, 457 (2010).

[53] G. L. Eyink, Stochastic flux freezing and magnetic dynamo, Phys. Rev. E **83**, 056405 (2011).

[54] G. Eyink, E. Vishniac, C. Lalescu, H. Aluie, K. Kanov, K. Bürger, R. Burns, C. Meneveau, and A. Szalay, Flux-freezing breakdown in high-conductivity magnetohydrodynamic turbulence, Nature (London) **497**, 466 (2013).